Zeeman-resolved Autler-Townes splitting in Rydberg atoms with tunable resonances and a single transition dipole moment

Noah Schlossberger [1,2,*] Andrew P. Rotunno [3] Alexandra B. Artusio-Glimpse [3] Nikunjkumar Prajapati [3] Samuel Berweger [3] Dangka Shylla [1,2] Matthew T. Simons [3] and Christopher L. Holloway [3]

[1]*Department of Physics, University of Colorado, Boulder, Colorado 80302, USA*
[2]*Associate of the National Institute of Standards and Technology, Boulder, Colorado 80305, USA*
[3]*National Institute of Standards and Technology, Boulder, Colorado 80305, USA*

Applying a magnetic field as a method for tuning the frequency of Autler-Townes splitting for Rydberg electrometry has recently been demonstrated. In this Letter, we provide a theoretical understanding of Rydberg electromechanically-induced-transparency signals of alkali metal atoms in the presence of a large magnetic field, as well as demonstrate some advantages of this technique over traditional Autler-Townes-based electrometry. We show that a strong magnetic field provides a well-defined quantization axis regardless of the optical field polarizations; we demonstrate that by separating the m_J levels of the Rydberg state, we can perform an Autler-Townes splitting with a single participating dipole moment, and we demonstrate recovery of signal strength by populating a single m_J level using circularly polarized light.

I. INTRODUCTION

Highly excited atomic Rydberg states in alkali atoms have been demonstrated as "self-calibrated" microwave field sensors [1–8] due to strong calculable [9] dipole matrix elements between Rydberg states. States are experimentally populated and probed by multiphoton electromagnetically induced transparency (EIT) [10], and field measurements are made by interpreting the laser absorption spectrum through an atomic vapor cell. Radio frequency fields can be measured via their induced Autler-Townes (AT) splitting of the Rydberg states, with the splitting proportional to the amplitude of the incident radiation field. Since each atomic species has a defined set of discrete transition frequencies, the ability to tune these transitions for measuring radiation at arbitrary frequency has been demonstrated using off-resonant measurements [11–15], as well as DC electric [16–19], AC electric [18,20–23], and DC magnetic [24–27] fields. Magnetically tuned Autler-Townes electrometry has been shown to demonstrate comparable minimum detectable fields to its untuned counterparts [26]. This work attempts to clearly illustrate some subtle aspects of Zeeman-tuned electrometry.

There are several key benefits to working in a strong magnetic field, i.e., a field such that $\mu_B B \gg \Omega$, where μ_B is the Bohr magneton, B is the applied magnetic field strength, and Ω is the larger of the Rabi rates of the probe and coupling lasers. In this regime, of the order of mT, the magnetic field defines the preferred quantization axis (i.e., the axis in which the angular momentum is a good quantum number and polarized light acts with standard selection rules when projected into this axis). In comparison to a Hamiltonian consisting of only photon interactions, this situation is much less ambiguous [generally, when $\mu_B B$ is small compared to the Rabi rates, a Rabi rate much stronger than the other Rabi rates can unambiguously set the quantization axis, e.g., the radio frequency (rf) photon in AT].

In the large-B regime, individual m_J levels of the Rydberg state in the EIT signal can be resolved, enabling direct observation of angular momentum dynamics that is valuable for polarization studies. Isolated m_J levels simplify Autler-Townes splitting, allowing calibration of electrometry using a single unambiguous transition dipole matrix element for a well-defined rf polarization.

In this Letter, we will add a theoretical foundation to the results presented in, e.g., [26,27], demonstrate that field-induced m_J selectivity leads to a unique AT dipole matrix element, and demonstrate that with circular polarized light, magnetically tuned AT electrometry can be performed with a similar signal strength as without a magnetic field. An understanding of the involved pathways that lead to the shape of these signals and leveraging the advantages shown in this Letter will ultimately lead to less ambiguous and more sensitive electric field measurements.

II. EIT IN THE PRESENCE OF A STRONG MAGNETIC FIELD

The energy-level diagram for a two-photon cascade EIT scheme and the rf extension for Rydberg Autler-Townes splitting is shown in Fig. 1. State $|1\rangle$ is the $S_{1/2}$ ground state's highest hyperfine manifold, state $|2\rangle$ is the $P_{3/2}$ state's highest hyperfine manifold, state $|3\rangle$ is a Rydberg $nD_{5/2}$ state, and state $|4\rangle$ is a nearby Rydberg state. The coupling laser is swept through resonance, with its detuning Δ_c defined as the difference between the photon energy E_γ and the spacing
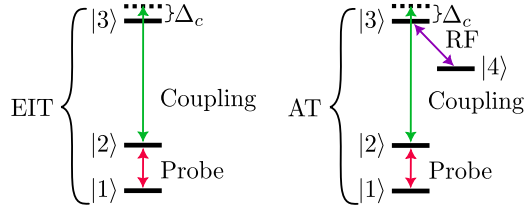
*noah.schlossberger@nist.gov

FIG. 1. Energy level schemes for Rydberg EIT and AT.

between the unperturbed energies of the $|2\rangle$ and $|3\rangle$ states,

$$\Delta_c \equiv \frac{E_\gamma - (E_{|3\rangle} - E_{|2\rangle})}{\hbar}, \tag{1}$$

where $\hbar$ is the reduced Planck constant.

A theoretical approach to treating the relevant states in an EIT or Autler-Townes scheme involves treating m_F as the quantum number describing the angular momentum in the low-principal quantum number states where $\mu_B B$ is small compared to the hyperfine energy splitting ($\sim$GHz in $|1\rangle$ and $\sim$100s of MHz in $|2\rangle$), and using m_J as the quantum number describing the angular momentum of the Rydberg states, where the hyperfine splitting is small compared to $\mu_B B$ and cannot be resolved. This treatment is sufficient because the m_I dependence of the Zeeman shift is negligible [28]. Note that for a large enough field, the intermediate $|2\rangle$ state will have similar strengths of hyperfine and Zeeman splittings, meaning neither treatment is sufficient [25]. The two pictures can be linked with selection rules acting on m_F in the lower states and $m_I + m_J$ in the Rydberg states, and summing over all m_I.

In the presence of a magnetic field, each level undergoes a shift in energy of

$$\Delta f = \frac{\mu_B B}{h} \times \begin{cases} g_F m_F, & \text{low-}n \text{ states} \\ g_J m_J, & \text{Rydberg states,} \end{cases} \tag{2}$$

where g_J and g_F are the Landé g factors as described in [29].

The transition dipole matrix element $d_{m_{F2}\to m_{J3}}$ from a hyperfine m_F state of $|2\rangle$ to a fine-structure m_J state of $|3\rangle$ is calculated by projecting the fine-structure state into its associated hyperfine states and summing over the dipole matrix element from each component,

$$
\begin{aligned}
d_{m_{F2}\to m_{J3}} &\equiv \langle n_2, L_2, J_2, F_2, m_{F2}|e\vec{r}|n_3, L_3, J_3, m_{J3}\rangle \\
&= \sum_{F'} \sum_{m'_F=-F'}^{F'} \sum_{m'_I=-I}^{I} C^{F'm'_F}_{Im'_I J_3 m_{J3}} \\
&\quad \times \langle n_2, L_2, J_2, F_2, m_{F2}|e\vec{r}|n_3, L_3, J_3, F', m'_F\rangle,
\end{aligned} \tag{3}
$$

where $C^{JM}_{j_1 m_1 j_2 m_2}$ are the Clebsch-Gordan coefficients, n is the principal quantum number, L is the orbital angular momentum quantum number, J is the total electronic angular momentum quantum number, F is total atom angular momentum quantum number, m_F and m_J are the projection of the the total electronic and total angular momenta, respectively, onto the quantization axis, and the number in the subscripts corresponds to the state as labeled in Fig. 1. Neglecting saturation effects, the relative total transition strength $P(m_{J3})$
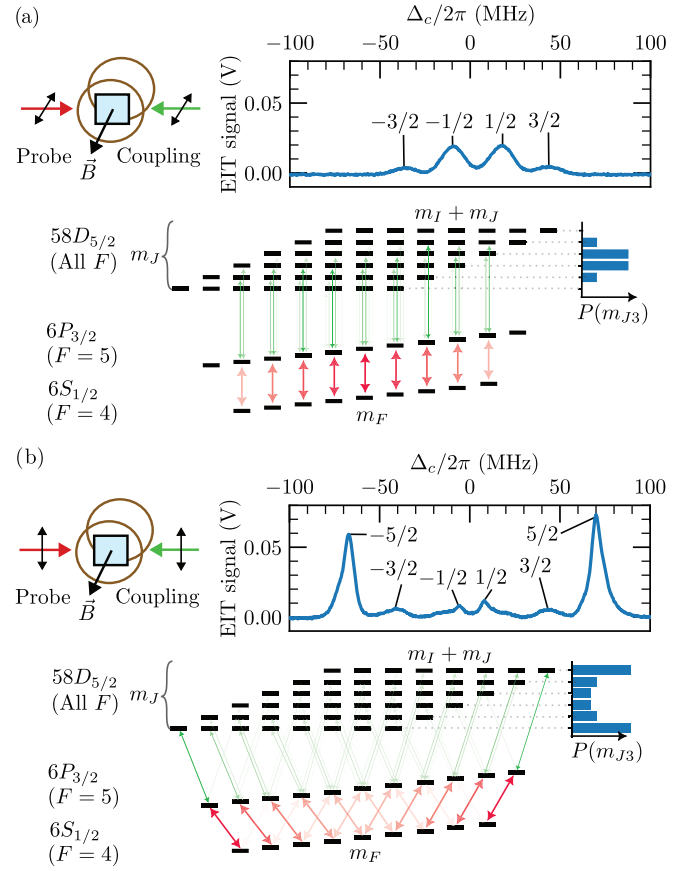

FIG. 2. Measured EIT signals in the presence of a strong [1.85(1) mT] magnetic field either (a) aligned with or (b) orthogonal to the polarization axis. For each case, the polarization and magnetic field axes are visualized in the top left, and the resulting EIT signal is shown in the top right, with each peak labeled by the m_J of its Rydberg state $|3\rangle$. The energy-level diagrams show the angular momentum pathways from the ground state to the various m_J levels, with the opacity of each transition scaled by the square of its transition dipole moment. To the right of the diagram are theoretical signal strengths $P(m_{J3})$ given by Eq. (4).

going to any different m_J level in the Rydberg $|3\rangle$ state is proportional to

$$P(m_{J3}) \propto \sum_{m_{F1}} \sum_{m_{F2}} d^2_{m_{F1}\to m_{F2}} d^2_{m_{F2}\to m_{J3}}. \tag{4}$$

The relative EIT peak intensities are approximately described by these probabilities, with complications arising from spontaneous emission and cycling transition rates. The theoretical transition dipole moments can be calculated using the ARC PYTHON package [9] neglecting Zeeman or Stark effects, which can modify atomic wave functions and associated transition dipole matrix elements [1].

In Fig. 2, an EIT signal is obtained on the $6S_{1/2}(F = 4) \to 6P_{3/2}(F = 5) \to 58D_{5/2}$ pathway in Cs, using the experimental setup detailed in Sec. VI. The coupling laser detuning scans around the atomic state resonance, while the probe remains fixed on the $|1\rangle \to |2\rangle$ transition. Shot-to-shot calibration is achieved through a field-free vapor cell measurement, with the zero of the coupling detuning defined by the $P_{3/2} \to D_{5/2}$

Rydberg EIT transition in the reference cell. The spacing between this peak and the $P_{3/2} \rightarrow D_{3/2}$ transition provides scaling calibration between the piezosweep location and frequency.

The magnetic field orientation significantly influences the distribution of the m_J peak strengths in the EIT signal. The magnetic field establishes the quantization axis, causing aligned laser polarizations to result in π transitions, while perpendicular orientations yield a superposition of σ^+ and σ^- polarizations along the quantization axis. Due to the stronger dipole moments for transitions bringing angular momentum towards the nearest extrema, the stretched states $m_J = \pm 5/2$ exhibit the strongest EIT signal in this scenario.

In the perpendicular case, the m_J peaks appear to have internal structure leading to unequal frequency spacing, and the $m_J = \pm 5/2, \pm 1/2$ peaks are narrower than the $m_J = \pm 3/2$ peaks. This can be understood by considering EIT pathways and population dynamics. Each possible transition pathway that shows up in the EIT signal has its own coupling laser frequency at which EIT will occur, which depends on the Zeeman shifts on all three associated states:

$$\Delta f(m_{F1}, m_{F2}, m_{J3})$$
$$= \frac{\mu_B B}{h} \left[\underbrace{g_{J_3} m_{J3} - g_{F_2} m_{F2}}_{\text{Coupling Shift}} + \underbrace{\frac{f_c}{f_p}(g_{F_2} m_{F2} - g_{F_1} m_{F1})}_{\text{Probe Doppler Shift}} \right],$$

(5)

where f_p and f_c are the frequencies of the probe and coupling lasers, respectively.

We can then theoretically construct the EIT signal by summing a finite-width Gaussian for each transition with its amplitude prescribed by the transition strength given by the product of the square of the transition dipole moments and its location prescribed by the Δf in Eq. (5). Further realism can be added by weighting each path by its initial ground-state likelihood. This can be written as

$$V(f) = \sum_{m_{F1}} \sum_{m_{F2}} \sum_{m_{J3}} n(m_{F1}) d^2_{m_{F1} \rightarrow m_{F2}} d^2_{m_{F2} \rightarrow m_J}$$
$$\times e^{\frac{-[f - \Delta f(m_{F1}, m_{F2}, m_{J3})]^2}{2\sigma^2}},$$

(6)

where $\{n(m_{F1})\}$ is the steady-state ground-state m_F distribution and σ is the empirical Gaussian width of each individual transition pathway (modeling the inhomogeneous broadening arising from the uncancelled portion of the Doppler shift on each atom and their thermal velocity distribution).

Calculations of this theoretical EIT signal for light polarization both parallel to and orthogonal to the magnetic field are shown in Fig. 3. The ground-state population distribution $\{n(m_{F1})\}$ is calculated using RYDIQULE [30] to numerically solve a many-state model. The model uses the Zeeman basis of $\{m_F, m_F, m_J\}$ for the $\{6S_{1/2}, 6P_{3/2}, 58D_{5/2}\}$ states, respectively, summing over m_I. The model accounts for Rabi scaling and decay branching between states using Zeeman-resolved dipole moments [9], sending all additional decay from the Rydberg state to all m_F sublevels of $|1\rangle$ equally. The laser field strengths expressed as Rabi frequency per dipole moment used in the model are a probe field of $0.8 \frac{\text{MHz}}{e \cdot a_0}$ and a coupling
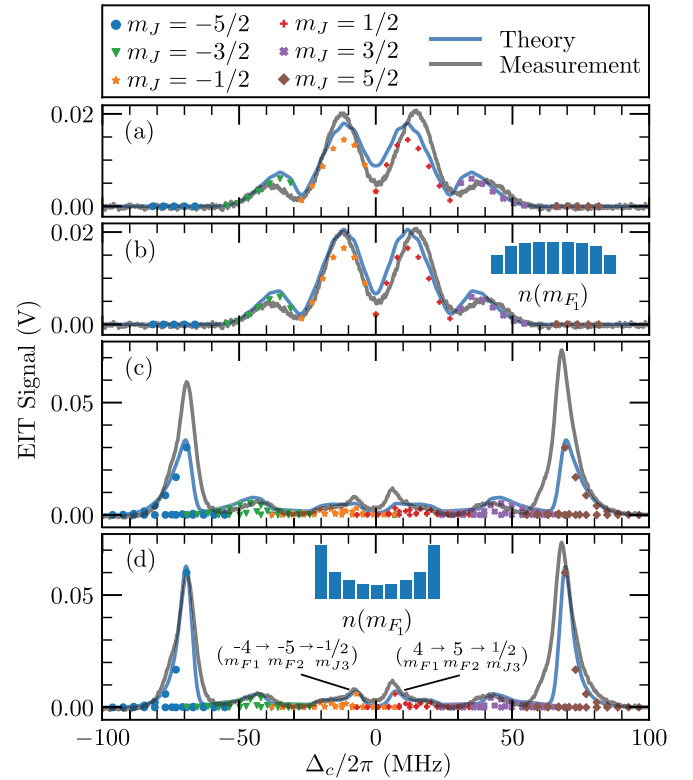

FIG. 3. Theoretical and measured EIT signals for Cs in the presence of a 1.85(1) mT magnetic field for light polarizations that are (a),(b) aligned with and (c),(d) perpendicular to the magnetic field. (a) and (c) present the theory from Eq. (6) assuming a uniform ground-state distribution, while (b) and (d) include population weighting from the steady-state model. The floated parameters are an overall amplitude scaling and the width σ of each transition, which is common among all four theory curves.

field of $80 \frac{\text{MHz}}{e \cdot a_0}$, calculated from the beam powers and sizes discussed in Sec. VI.

The dipole moments alone are able to capture the general shape of the waveforms, while adding in the $n(m_F)$ weights captures the fact that with spontaneous emission, π-polarized light generally moves the population towards lower $|m_F|$ states, while $(\sigma^+ + \sigma^-)$-polarized light generally moves the population towards higher $|m_F|$ states.

Generally, this theory explains the shapes of each m_J peak in the EIT signal in the presence of a strong magnetic field and indicates that each peak predominantly corresponds to a pure m_J level in the Rydberg state. It is also notable that in the parallel polarization case, the apparent width of each m_J peak predominantly comes from Zeeman-induced spread in the resonant coupling frequencies [Eq. (5)] for each pathway [see Fig. 3(b)].

The parallel polarization case is impractical for electrometry due to broad peaks arising from numerous angular momentum pathways. In contrast, perpendicular polarization yields narrower peaks and stronger signals, as most of the population resides in the outer two states. Other polarization combinations with orthogonal probe and coupling polarizations exhibit characteristics between these extremes.
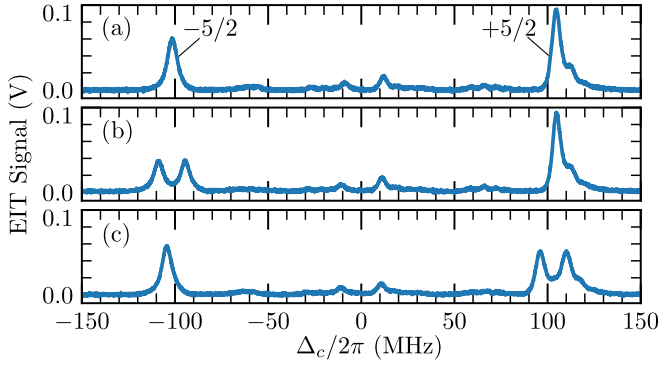
FIG. 4. Measured Autler-Townes splittings in individual m_J levels via the $58D_{5/2}(m_J = \pm 5/2) \rightarrow 59P_{3/2}(m_J = \pm 3/2)$ transitions of Cs in the presence of 2.78(1) mT. (a) No rf is applied. (b) An rf frequency of 3.5426 GHz is applied. (c) An rf frequency of 3.6205 GHz is applied. The frequency difference of 77.9 MHz between (b) and (c) corresponds to $2\mu_B B$.

III. AUTLER-TOWNES

To find the shift in the microwave frequency at which resonant Autler-Townes splitting will occur, one can simply subtract the Zeeman shifts on the m_J levels of the two Rydberg states,

$$\Delta f = (g_{J4}m_{J4} - g_{J3}m_{J3})\frac{\mu_B B}{h}. \qquad (7)$$

It is worth noting that if the fourth state is lower in energy than the third state, this apparent Δf changes sign since the microwave resonance corresponds to the *magnitude* of the energy difference. For the stretched transition from a $(n)D_{5/2}$ to a lower-energy $(n+1)P_{3/2}$ state, the shift in the frequency at which the Autler-Townes is sensitive to is given by

$$\Delta f = -\left(g_{P_{3/2}}\frac{3}{2} - g_{D_{5/2}}\frac{5}{2}\right)\frac{\mu_B B}{h} = \frac{\mu_B B}{h}, \qquad (8)$$

which gives a shift of 13.996 MHz per mT of magnetic field. Note that the difference of $m_J g_J$ products simplifies to 1 for a stretched state transition.

Using the optical fields perpendicular to the magnetic field populates the $m_J = \pm 5/2$ states of the Rydberg level, in which the Zeeman-induced shift of the Autler-Townes frequency is maximized. In this configuration, we can independently split the $m_J = -5/2$ and $+5/2$ levels at different microwave frequencies, as demonstrated in Fig. 4.

Lifting m_J-level degeneracy in Rydberg states simplifies Autler-Townes splittings to a single dipole moment. Conventional Autler-Townes electrometry [2] uses aligned linearly polarized fields for π transitions, but multiple populated m_J levels lead to simultaneous splittings with different dipole moments. This complicates calibration, as effective splittings depend on nontrivial steady-state population dynamics.

For a $D_{5/2} \rightarrow P_{3/2}$ transition, there are two unique dipole elements to account for for π microwaves ($m_J = \pm 1/2 \leftrightarrow \pm 1/2, \pm 3/2 \leftrightarrow \pm 3/2$) and four more for unintended σ transitions, while for a $D_{5/2} \rightarrow F_{7/2}$ transition, there
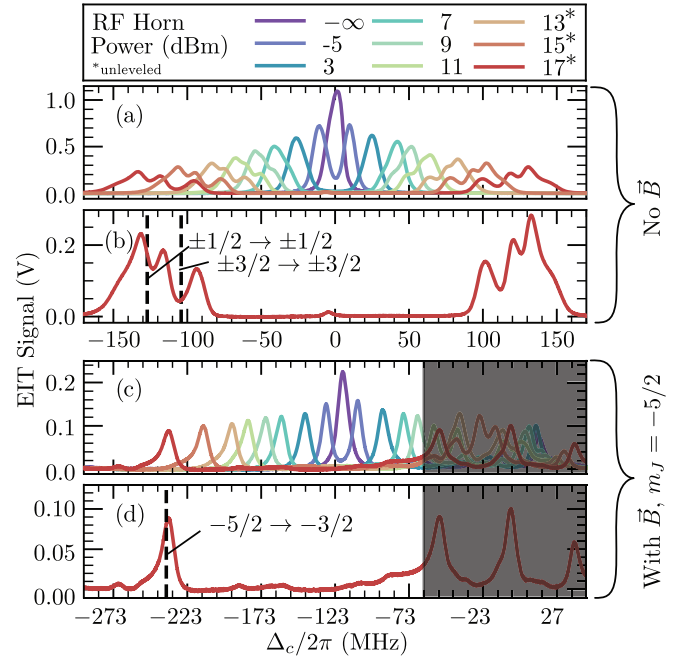

FIG. 5. Measured Autler-Townes splittings on the Cs $58D_{5/2} \rightarrow 59P_{3/2}$ transition. (a),(b) No magnetic field is applied, and optical and rf fields share the same polarization axis. (c),(d) 3.24(1) mT of magnetic field is applied orthogonal to the rf and optical polarization axis, and the $m_J = -5/2$ hyperfine state is split. The area in which other m_J levels start to interfere with the right Autler-Townes peak at high rf fields is grayed out. (b) and (d) show the EIT signals with 17 dBm going into the horn, corresponding to $\sim$3 V/m of rf applied to the atoms. The theoretical AT peak locations corresponding to each relevant dipole moment are marked with a dashed vertical line.

are three unique dipoles for π transitions and six more for unintended σ transitions.

In contrast, applying a magnetic field large enough to separate the m_J levels means that when Autler-Townes is performed, the number of transitions reduces to one for pure microwave polarization and, at most, two more for mixed polarization, and these will be off-resonant when tuned to a particular $m_J \rightarrow m_{J'}$ transition. A particularly clean transition is the $D_{5/2}(m_J = 5/2) \rightarrow P_{3/2}(m_J = 3/2)$ stretched state transition, in which only a single transition is allowed from the initial state. This is demonstrated in Fig. 5.

In the no-magnetic-field case with aligned linearly polarized light (the standard case for Rydberg AT electrometry), the signal is difficult to interpret, but it is clear that the AT peaks spread out and have structure as the microwave field increases amplitude, while the m_J-resolved case stays narrow at high field, indicating it is being split by a single transition.

This makes isolating m_J levels with a magnetic field an appealing option for precision electrometry using Rydberg atom sensors, with the potential drawbacks being interference of the microwave field by the geometry of the magnetic field sources, as well as potential reduction in signal strength, which can be avoided with circularly polarized light, as demonstrated in the next section.
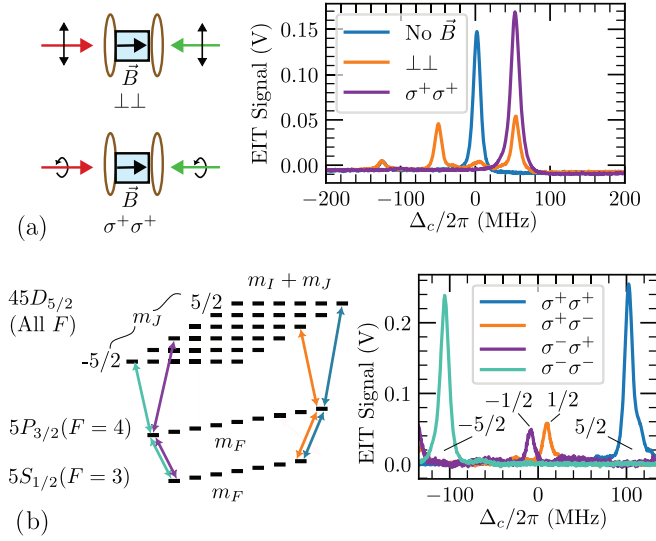
FIG. 6. EIT in the presence of a large magnetic field using circularly polarized light. (a) Recovery of the measured EIT signal strength on ^{85}Rb in a magnetic field of 1.39(1) mT by using circular polarized light to populate $m_J = 5/2$ instead of linearly polarized light. The peak height exceeds that of the no-magnetic-field case. (b) Measured EIT signals on ^{85}Rb in a magnetic field of 2.78(1) mT under the four possible combinations of circularly polarized probe and coupling light with respect to the magnetic field axis. The polarizations are labeled as the probe polarization, then the coupling polarization. Left: The predominant transition pathway for each polarization combination. Right: The resulting EIT signals for each polarization combination, with each peak labeled the m_J of its Rydberg state $|3\rangle$.

IV. POLARIZATION

In Fig. 2, we saw that different linear polarizations lead to EIT in different m_J levels, with the most useful case being polarization perpendicular to the magnetic field direction because it excites the stretched states, which have the most disparate rf resonances. However, each m_J peak is significantly weaker than the standard EIT peak without a magnetic field since the population is split between the $+5/2$ and $-5/2$ states. This signal reduction ultimately reduces the minimum detectable field using this technique.

The signal strength can be recovered by rotating the magnetic field to be aligned with the propagation axis of the lasers and using circularly polarized light. In this way, the entire population can be pumped to the $m_J = +5/2$ level, actually resulting in a slight increase in the resulting signal over the standard technique due to the higher transition dipole moments of σ transitions compared to π transitions. This is demonstrated in the $5S_{1/2}(F = 3) \rightarrow 5P_{3/2}(F = 4) \rightarrow 45D_{5/2}$ transition in ^{85}Rb in Fig. 6(a).

Special care was taken to avoid polarization-dependent effects in the measurement, such as using pickoff mirrors to overlap the probe and coupling beams at a slight angle rather than a dichroic, which would have polarization-dependent transmittance. In addition, all four possible combinations of polarized light can populate various isolated m_J levels, as depicted in Fig. 6(b).
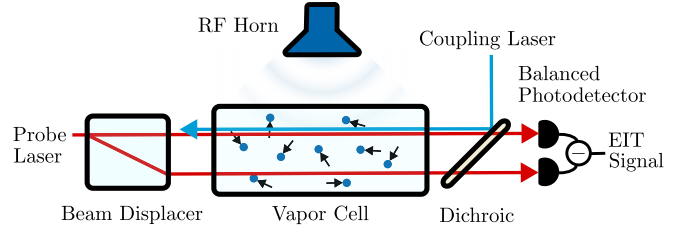

FIG. 7. The experimental setup for measuring EIT and AT.

V. CONCLUSION

We have made several useful observations about the use of mT-scale magnetic fields in order to tune Autler-Townes electrometry. First, we made sense of the shape of the EIT signals theoretically and demonstrated that the magnetic field defines the quantization axis. Next, we have demonstrated that isolating m_J levels via Zeeman splitting leads to Autler-Townes splittings with a single transition and therefore a single dipole moment, thus making rf power calibration simpler. Finally, we have demonstrated in Fig. 6(a) that we can perform this technique with the same or a greater signal-to-noise ratio as without a magnetic field using circularly polarized light.

VI. METHODS

The experimental setup used for measuring the EIT and AT spectra is shown in Fig. 7.

The probe is split into two beams: one overlaps with the coupling beam to sample resonant absorption minus electromagnetically induced transmittance, and the other passes through the cell independently to sample only resonant absorption. The balanced photodetector detects the difference in transmittance, isolating the EIT signal from background absorption. The counterpropagating direction of the beams partially cancels the Doppler shift of each atom, resulting in a narrower EIT linewidth than the Doppler linewidth.

The Cs atoms are in a 25-mm-diameter by 25-mm-length vapor cell, and the Rb atoms are in a 25-mm-diameter by 75-mm-length cell. Both cells are at room temperature, with an atomic gas density at saturation and an internal background gas pressure lower than 10^{-6} Pa. The rf is applied with a broadband horn placed $\sim$54 cm from the cell.

The probe laser (780 nm for Rb and 852 nm for Cs) is an external cavity diode laser (ECDL) with a power of the order of 10 µW and locked to a reference atomic vapor cell using saturated absorption spectroscopy. The coupling laser (480 nm for Rb and 509 nm for Cs) is an ECDL with a tapered amplifier with a power of the order of 80 mW. Both photons have $\sim$10 kHz linewidths, with beams of one-σ Gaussian widths of the order of 500 µm.

The choice of Cs and Rb was made for experimental convenience, with Cs used in Figs. 2–5 because our Cs system has a higher signal-to-noise ratio and Rb in Fig. 6 because of the on-hand availability of the required polarization optics.

The magnetic field is applied with a proprietary set of Helmholtz coils with a coil diameter of 195 mm and of the order of 200 turns, with a nominal internal magnetic

field of 1 mT/A but measured via Zeeman splitting to be 0.926(1) mT/A at the center of the apparatus, varying by less than 10% within the active region of the coil pair. The magnetic field values are reported as the applied current multiplied by this ratio. Background magnetic fields (<0.1 mT) are small compared to applied fields, so their effects are not included, but a 0.1 mT uncertainty is included in the error analysis.

The data relevant to the findings of this research project are available at [31].

[1] J. A. Sedlacek, A. Schwettmann, H. Kübler, R. Löw, T. Pfau, and J. P. Shaffer, Nat. Phys. **8**, 819 (2012).

[2] C. L. Holloway, J. Gordon, A. Schwarzkopf, D. Anderson, S. Miller, N. Thaicharoen, and G. Raithel, IEEE Trans. Antenna Propag. **62**, 6169 (2014).

[3] A. Artusio-Glimpse, M. T. Simons, N. Prajapati, and C. L. Holloway, IEEE Microwave Mag. **23**, 44 (2022).

[4] C. L. Holloway, M. T. Simons, J. A. Gordon, A. Dienstfrey, D. A. Anderson, and G. Raithel, J. Appl. Phys. **121**, 233106 (2017).

[5] D. H. Meyer, Z. A. Castillo, K. C. Cox, and P. D. Kunz, J. Phys. B: At., Mol. Opt. Phys. **53**, 034001 (2020).

[6] C. T. Fancher, D. R. Scherer, M. C. S. John, and B. L. S. Marlow, IEEE Trans. Quantum Eng. **2**, 1 (2021).

[7] J. Yuan, W. Yang, M. Jing, H. Zhang, Y. Jiao, W. Li, L. Zhang, L. Xiao, and S. Jia, Rep. Prog. Phys. **86**, 106001 (2023).

[8] B. Liu, L. Zhang, Z. Liu, Z. Deng, D. Ding, B. Shi, and G. Guo, Electromag. Sci. **1**, 1 (2023).

[9] N. Šibalić, J. D. Pritchard, C. S. Adams, and K. J. Weatherill, Comput. Phys. Commun. **220**, 319 (2017).

[10] A. K. Mohapatra, T. R. Jackson, and C. S. Adams, Phys. Rev. Lett. **98**, 113003 (2007).

[11] M. T. Simons, J. A. Gordon, C. L. Holloway, D. A. Anderson, S. A. Miller, and G. Raithel, Appl. Phys. Lett. **108**, 174101 (2016).

[12] M. T. Simons, A. B. Artusio-Glimpse, C. L. Holloway, E. Imhof, S. R. Jefferts, R. Wyllie, B. C. Sawyer, and T. G. Walker, Phys. Rev. A **104**, 032824 (2021).

[13] D. A. Anderson and G. Raithel, Appl. Phys. Lett. **111**, 053504 (2017).

[14] J. Hu, H. Li, R. Song, J. Bai, Y. Jiao, J. Zhao, and S. Jia, Appl. Phys. Lett. **121**, 014002 (2022).

[15] D. H. Meyer, P. D. Kunz, and K. C. Cox, Phys. Rev. Appl. **15**, 014053 (2021).

[16] A. Osterwalder and F. Merkt, Phys. Rev. Lett. **82**, 1831 (1999).

[17] L. Ma, M. A. Viray, D. A. Anderson, and G. Raithel, Phys. Rev. Appl. **18**, 024001 (2022).

[18] C. L. Holloway, N. Prajapati, J. A. Sherman, A. Rüfenacht, A. B. Artusio-Glimpse, M. T. Simons, A. K. Robinson, D. S. La Mantia, and E. B. Norrgard, AVS Quantum Sci. **4**, 034401 (2022).

[19] A. Duspayev, R. Cardman, D. A. Anderson, and G. Raithel, arXiv:2310.10542.

[20] M. W. Noel, W. M. Griffith, and T. F. Gallagher, Phys. Rev. A **58**, 2265 (1998).

[21] P. Bohlouli-Zanjani, J. A. Petrus, and J. D. D. Martin, Phys. Rev. Lett. **98**, 203005 (2007).

[22] S. Berweger, N. Prajapati, A. B. Artusio-Glimpse, A. P. Rotunno, R. Brown, C. L. Holloway, M. T. Simons, E. Imhof, S. R. Jefferts, B. N. Kayim *et al.*, Phys. Rev. Appl. **19**, 044049 (2023).

[23] A. P. Rotunno, S. Berweger, N. Prajapati, M. T. Simons, A. B. Artusio-Glimpse, C. L. Holloway, M. Jayaseelan, R. M. Potvliege, and C. S. Adams, J. Appl. Phys. **134**, 134501 (2023).

[24] S. Bao, H. Zhang, J. Zhou, L. Zhang, J. Zhao, L. Xiao, and S. Jia, Phys. Rev. A **94**, 043822 (2016).

[25] J. Naber, A. Tauschinsky, B. van Linden van den Heuvell, and R. Spreeuw, SciPost Phys. **2**, 015 (2017).

[26] Y. Shi, C. Li, K. Ouyang, W. Ren, W. Li, M. Cao, Z. Xue, and M. Shi, Opt. Express **31**, 36255 (2023).

[27] X. Li, Y. Cui, J. Hao, F. Zhou, Y. Wang, F. Jia, J. Zhang, F. Xie, and Z. Zhong, Opt. Express **31**, 38165 (2023).

[28] F.-D. Jia, H.-Y. Zhang, X.-B. Liu, J. Mei, Y.-H. Yu, Z.-Q. Lin, H.-Y. Dong, Y. Liu, J. Zhang, F. Xie, and Z.-P. Zhong, J. Phys. B: At., Mol. Opt. Phys. **54**, 165501 (2021).

[29] D. A. Steck, Cesium D line data (unpublished).

[30] B. N. Miller, D. H. Meyer, T. Virtanen, C. M. O'Brien, and K. C. Cox, Comput. Phys. Commun. **294**, 108952 (2024).

[31] N. Schlossberger, Data associated with "Zeeman-resolved Autler-Townes splitting in Rydberg atoms with a tunable RF resonance and a single transition dipole moment", National Institute of Standards and Technology (2023), https://doi.org/10.18434/mds2-3102.